Composites Part B 201 (2020) 108377

Contents lists available at ScienceDirect

Composites Part B

journal homepage: www.elsevier.com/locate/compositesb

Protein-based flexible thermal conductive materials with continuous network structure: Fabrication, properties, and theoretical modeling

Ye Xue [a,b], Samuel Lofland [a], Xiao Hu [a,b,c,*]

[a] Department of Physics and Astronomy, Rowan University, Glassboro, NJ, 08028, USA
[b] Department of Biomedical Engineering, Rowan University, Glassboro, NJ, 08028, USA
[c] Department of Molecular and Cellular Biosciences, Rowan University, Glassboro, NJ, 08028, USA

ARTICLE INFO

Keywords:
Thermal conductivity
Thermal expansion
Dielectric constant
Silk fibroin
Aluminum nitride
Renewable biocomposite

ABSTRACT

Protein is an ideal alternative to many synthetic components in green and bio-electronic products due to its natural abundance, high flexibility and excellent biocompatibility. Here, we report the development of new renewable thermal management materials based on a stable composite system of biocompatible silk fibroin (SF) protein with a small amount (≤25 vol%) of AlN inclusions. The self-assembly of AlN particles and SF was promoted by water annealing to enhance the hydrogen bonding between the phases to reduce the phonon scattering at the interface. The synthesized protein composites have excellent thermal stability, high mechanical durability and low linear expansion, related in part to the secondary structure of silk protein which can be modulated by changing the AlN content. The physical properties were analyzed and modeled within effective medium theory, and the agreements were reasonable, except for the thermal conductivity which was surprisingly much larger than predicted by the model (e.g. 5 times greater at 15 vol%), which is attributed to the strong interaction between protein and AlN, the high thermal conductivity of AlN, and the continuous network of AlN particles that formed at higher concentrations. This makes proteins excellent candidates for thermally conductive composite materials, which have many emerging applications in implantable biomedical devices, flexible and sustainable sensors, and green heat transfer products.

1. Introduction

Since the development of integrated circuit technology, the dimensions of electronic devices have continued to shrink while the power density is gradually increasing. Consequently, there has been increased effort to develop renewable or biocompatible materials with high thermal conductivity to serve as substrates to mitigate heating [1–9]. The ideal material should have good thermal conductivity, but it must also be electrically insulating and possess a low coefficient of thermal expansion. Because of their strong bonding, novel 1D and 2D materials such as BN, carbon nanotubes and graphene, show promising applications in thermal management [3,10–13]. The thermal conductivity of single-layer graphene at room temperature can reach 1800 W $m^{-1}K^{-1}$ [14,15] while the thermal conductivity of multi-walled nanotubes can be as high as 3000 W $m^{-1}K^{-1}$ [16]. However, the electrical conductivity of these carbon phases limits their use as thermal management materials for electronics [1,10,17].

Aluminum nitride is an electrical insulator with high thermal conductivity (320 W $m^{-1}K^{-1}$) but also has a low dielectric constant, a very wide bandgap of about 6.2 eV, a low thermal expansion coefficient (4.4 ppm K^{-1}), and stable chemical properties [18–21]. However, unlike polymers, ceramic AlN does not have enough strength or flexibility for many applications. On the other hand, the properties of silk include high tensile strength, elasticity, toughness, environmental friendliness, biocompatibility and insolubility (in most solvents) [22], which make it attractive for use in a range of fields, from dietary applications to biomedical devices. Many of properties of silk can be attributed to the fact that it is a protein polymer, yet polymers typically have a thermal conductivity of about 0.1 W $m^{-1}K^{-1}$ [15,23–25], rendering them impractical for thermal management applications.

One alternative is the synthesis of composite materials which can display the salient properties of its component materials. The properties of composites can be modulated by the size, distribution, and orientation of particles within a matrix, which may often be a polymer. For electrically insulating thermal management composites, the heat is transported by phonons, and studies have shown that the filler content and the interface between the filler and the matrix are the main factors affecting the thermal conductivity with interfacial scattering of phonons often dominating the thermal resistance [23,26].

* Corresponding author. Department of Physics and Astronomy, Rowan University, Glassboro, NJ, 08028, USA.
E-mail address: hu@rowan.edu (X. Hu).

https://doi.org/10.1016/j.compositesb.2020.108377
Received 21 February 2020; Received in revised form 3 August 2020; Accepted 19 August 2020
Available online 26 August 2020

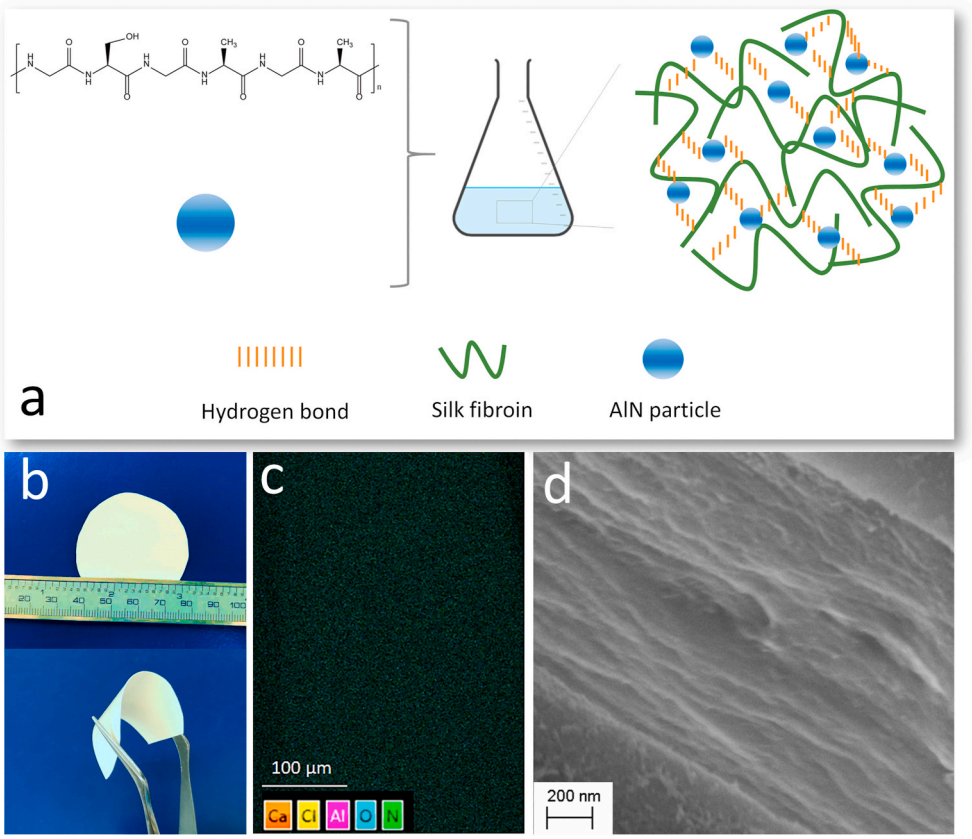

Fig. 1. (a) Schematic of preparation of AlN/SF solution, and the interaction between AlN particles and SF chains. (b) Photos of flexible 15% AlN/SF film. (c) Ca, Cl, Al, O and N EDS mapping of pure SF film shows the only measurable signal was from O and N. (d) Scanning electron micrograph of the cross section of the 2% AlN/SF sample.

Silk fibroin (SF) has a large number of hydroxyl groups on the protein chains, and these hydroxyl groups can form stable hydrogen bonds with the N atoms of the AlN. This may reduce the direct thermal resistance of the interface between SF and AlN particles [27–29]. In addition, the SF chain consists of both negatively (aspartic acid and glutamic acid) and positively (arginine and lysine) charged amino acid groups which may also reduce the interfacial phonon scattering [30]. At the same time, the secondary structure of the silk material can be more easily modified to achieve desired mechanical and structural properties than many polymer materials [22], which makes it advantageous to serve as a matrix.

Here we report on the structural and physical properties of SF and AlN composites. This composite material has the advantages of its constituent materials: excellent mechanical properties, biocompatibility and green environmental properties of SF protein, as well as the excellent high-temperature thermal stability, improved thermal conductivity and fire resistance of AlN. Based on the thermal and microstructural studies, AlN particles can form continuous networks that confine the crystalline and amorphous parts of silk proteins, which contribute to the good thermal stability and high thermal conductivity of AlN/SF films. Due to these advantages, SF and AlN composites have sizable potential for applications in high performance microelectronic devices and implantable biomedical electronic devices.

2. Material and methods

2.1. Materials and synthesis

Bombyx mori mulberry (Mori) silks were purchased from Treenway Silks (Colorado, USA). Silkworm cocoons were first boiled in a 0.02 M $NaHCO_3$ (Sigma-Aldrich, USA) solution for 30 min and then rinsed thoroughly with deionized water three times to completely remove the sericin from the fiber. The degummed silks were dried overnight in a fume hood and further dried in vacuum at room temperature for 1 day to remove the remaining moisture. The obtained pure SF fibers were dissolved in a formic acid solution with 4 wt% $CaCl_2$ at room temperature. The densities of dry state SF films and AlN particles (Sigma-Aldrich, USA; with mean particle size of 1.4 μm) were measured to be 1.4 and 3.26 g/cm^3, respectively. AlN was added into the SF solution at different ratios so that the resulting composites had a volume fraction of AlN of up to 25%. Henceforth, samples are designated as *x*% AlN/SF where *x* represents the percent volume fraction of AlN. The mixture solution was stirred by a vortex mixer for 10 min and then slowly cast onto polydimethylsiloxane (PDMS) substrates to form films. After drying in a hood for 2 days, the AlN/SF films were annealed in deionized water for 1 h to remove formic acid and $CaCl_2$ residues, to promote crystallization of the SF, and to enhance the formation of hydrogen bonding between the SF matrix and AlN particles. The water-annealed samples were left in a 30 °C vacuum oven to dry for 2 days before testing.

2.2. Characterization

Structural and microstructural studies were done by several techniques. Fourier transform infrared (FTIR) spectroscopy (Bruker Tensor 27, USA) was used to characterize the secondary structures of SF within the composite material [31]. The spectrometer was equipped with a deuterated triglycine sulfate detector and a multiple-reflection horizontal MIRacle ATR attachment (Ge crystal) from Pike Tech (Madison, WI). The instrument was continuously purged with N_2 gas to eliminate the spectral contributions of atmospheric water vapor. For each measurement, 128 scans were co-added with a resolution of 4 cm^{-1}. A LabRAM HR Evolution Raman Spectrometer (HORIBA Scientific, USA) with a 600 lines/mm grating was also used to analyze the protein

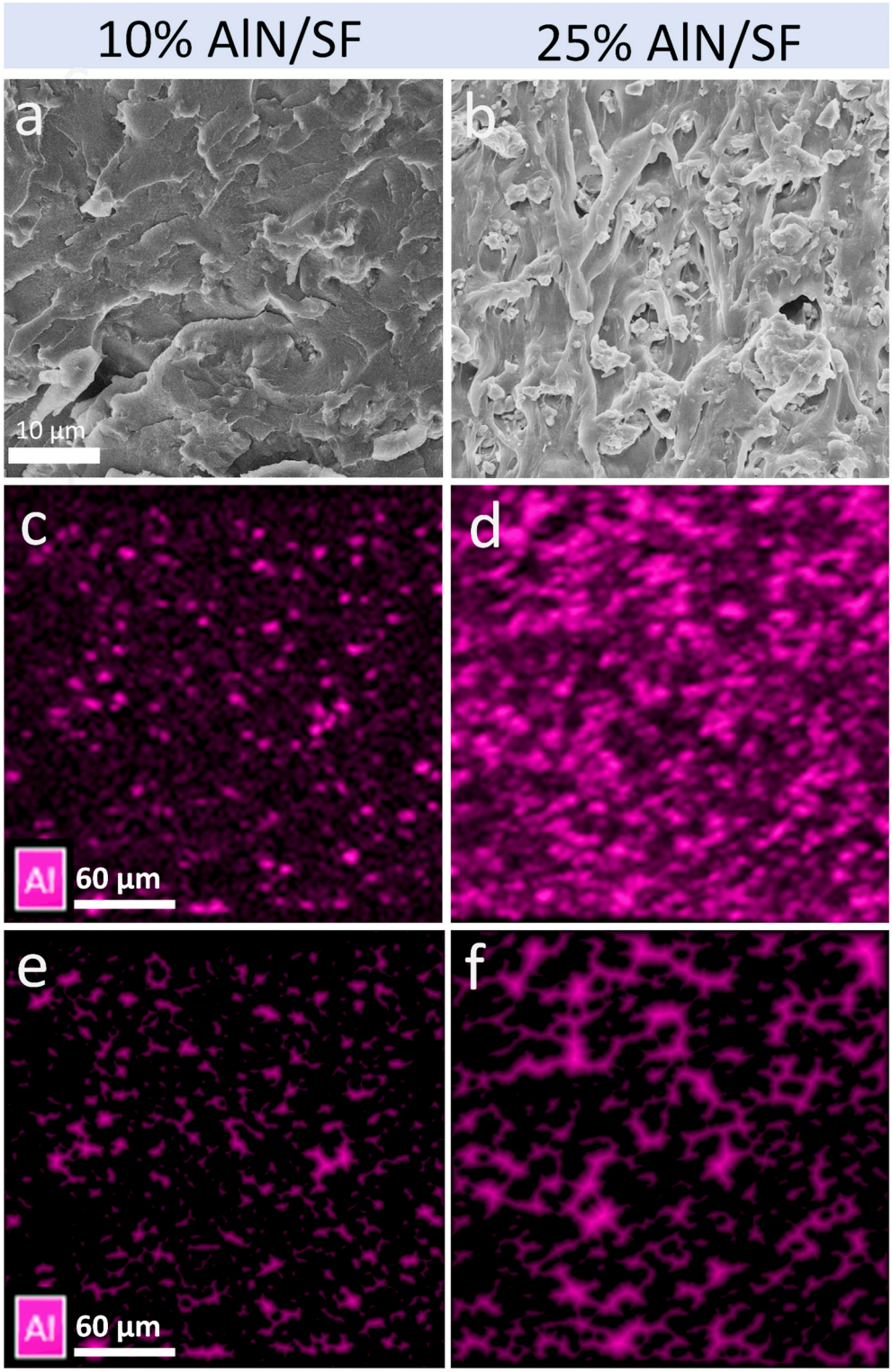

Fig. 2. Cross-sectional SEM images of (a) 10% AlN/SF, (b) 25% AlN/SF. EDS Al element mapping in (c) 10% AlN/SF, and (d) 25% AlN/SF. (e) and (f) show the morphological distance maps of the Al composition for 10% AlN/SF and 25% AlN/SF, respectively.

structure of different silk composites. Measurements were taken with a 785 nm laser with an incident power of ~10 mW, an exposure time of 300 s, for 3 accumulations for Raman shifts ranging from 500 cm^{-1} to 1800 cm^{-1}. Wide-angle X-ray scattering (WAXS) was performed with a Panalytical Empyrean X-ray diffractometer. The setup included a fixed anode X-ray source for Cu Kα radiation (wavelength $\lambda = 0.154$ nm), operating at 45 kV and 40 mA. The scattering angle 2θ ranged from 5° to 70°, and data were taken in steps of 0.013° with a hold time of 30 s/step. Measurements were taken as a function of the film orientation with the sample plane being rotated from 0° to 90° with respect to the incident beam (see Fig. 3d). X-ray diffraction (XRD) was also done with the same instrument in Bragg-Bretano geometry with similar operating parameters. The cross-section morphology of the AlN/SF films was characterized with a LEO ZEISS 1530 V P scanning electron microscope

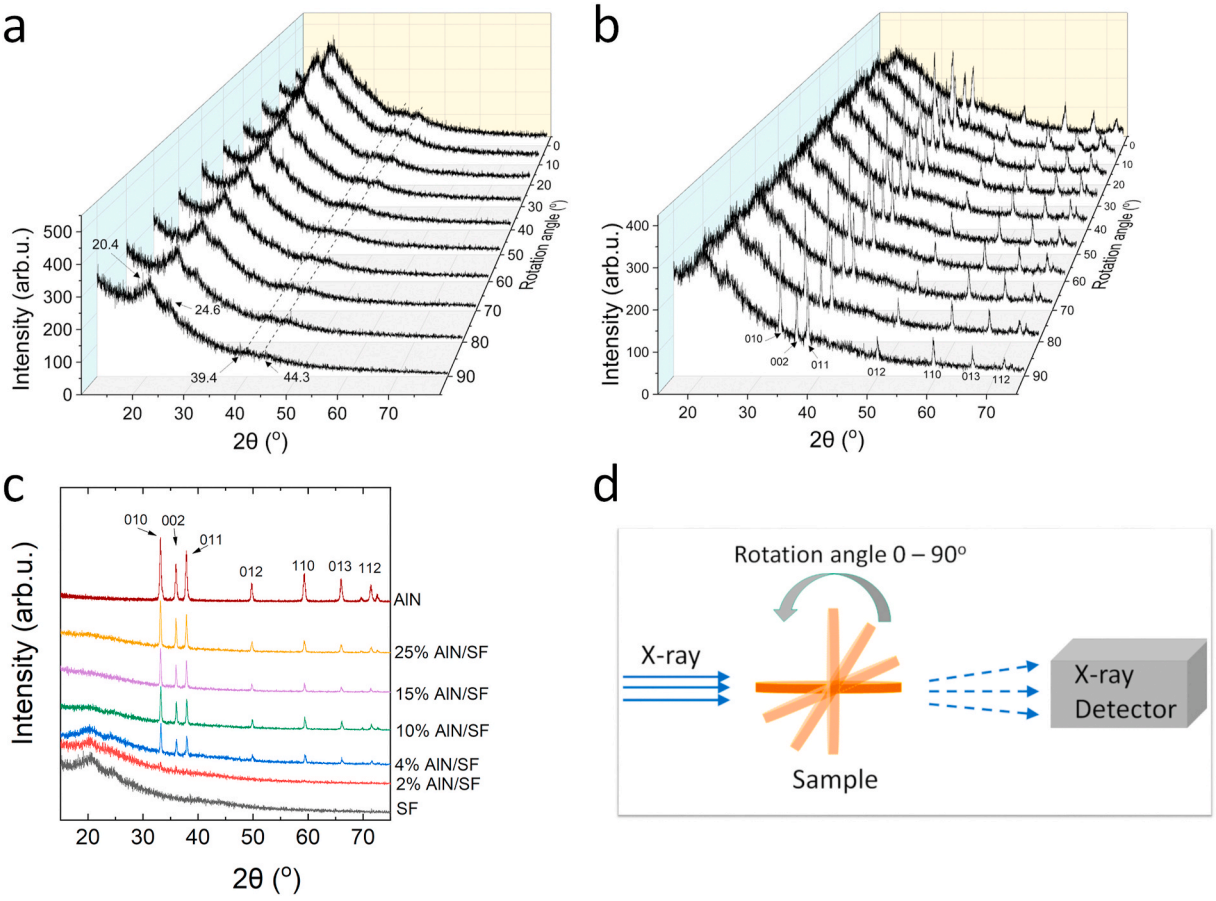

Fig. 3. WAXS patterns of (a) SF and (b) 4% AlN/SF films at different orientations. (c) XRD patterns of the SF, AlN/SF and AlN samples. (d) Scattering geometry.

(Oberkochen, Germany). The acceleration voltage was varied between 5 and 20 kV depending on the magnification. The elemental distribution of AlN was characterized by energy dispersive X-ray spectroscopy (EDS, Oxford Instruments).

Various methods were used to investigate the physical properties. Differential scanning calorimetry (DSC) was performed with a Q100 calorimeter (TA Instruments) equipped with a refrigerated cooling system. The N_2 flow rate was set to 50 ml/min, and measurements started at −30 °C and ended at 400 °C. The temperature increased at a rate of 2 °C/min and was modulated every 60 s at an amplitude of 0.318 °C to measure the reversing heat capacity. The decomposition behavior was analyzed by thermogravimetric analysis (TGA) on a TA Instruments SDT Q600 at a heating rate of 10 °C min^{-1} from 25 to 800 °C with an a gas flow of 100 ml/min of N_2. Linear thermal expansion was measured by a Q400 (TA Instruments) thermal mechanical analyzer (TMA) from 25 to 120 °C at a scan rate 10 °C/min. The sample was pre-loaded with 50 mN of force. The infrared thermal images were taken with a Seek Reveal thermal imaging camera (California, USA). The in-plane thermal conductivity was measured with a Physical Property Measurement System (Quantum Design, USA) with the thermal transport option (TTO) under steady-state conditions. Leads were attached with silver epoxy to a film sample with an area of 5 × 20 mm, and measurements were taken at vacuum below 9 × 10^{-5} Torr. The dielectric constant and loss were measured with an Agilent 4285 A Precision LCR Meter (Agilent, USA).

Parallel flame testing was performed on pure SF and 25% AlN/SF films. The size of the sample was 20 mm in length and 6 mm in width. A propane torch was used, and the samples were heated by flame until completely burned.

3. Results and discussion

3.1. Morphology and structure

Silk fibroin solutions were prepared according to our previously reported method [32]. Fig. 1b shows the 15% AlN/SF film, which is uniform in thickness and very flexible and shows no signs of mechanical fatigue even after being bent 90° over 50 times. The excellent mechanical properties is attributed to the strong hydrogen bonding interaction and electrostatic interaction between AlN and SF chains [33] (Fig. 1a and b). EDS was used to check the spatial distribution of various elements in the composites and demonstrates that there was no $CaCl_2$ left in any of the samples after water annealing (Fig. 1c and Fig. S1). In addition, the distribution of AlN is nearly homogeneous after annealing although there is some indication the particles are interconnected (Fig. 1c and Fig. S1).

SEM was used to study the internal structure and morphology of the matrix. We found layer-by-layer structures in all of the samples, which was induced by water annealing processing and silk-AlN molecular interactions (Fig. 1d and Fig. S2) [34–37]. As the concentration of AlN increased, more AlN particles were found in the cross section of the sample (Fig. 2a and b) which led to larger interconnected networks (Fig. 2e and f).

Previous studies have shown that water annealing can induce the crystallization of SF materials [38], so the orientation of β-sheet crystals and AlN particles was studied by WAXS. Those results demonstrate that both β-sheet and AlN crystallites are randomly oriented (Fig. 3a & b, Fig. S3) which suggests that the layered structure observed in SEM was

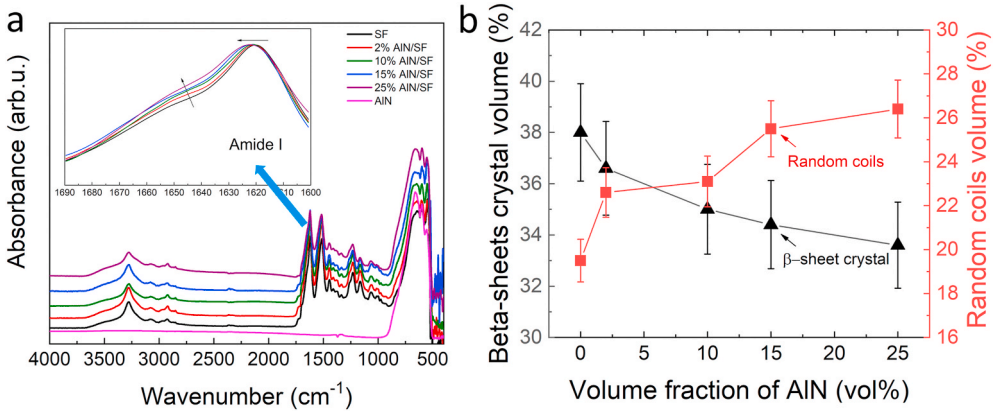

Fig. 4. (a) FTIR curves of water-annealed SF, AlN/SF films and AlN with the inset magnifying the amide I region of SF. (b) Volume fraction of β-sheet crystals and random coils of SF as a function of AlN.

separate from the crystal orientation and distribution in the material. The main x-ray diffraction peaks for AlN are consistent with the literature (JCPDS card No. 25–1133) [39], with 2θ values of 33.2°, 35.9°, 37.9°, 49.8°, 59.3°, and 65.9° assigned to the (010), (002), (011), (012), (110), and (013) reflections, respectively (Fig. 3c). Pure SF (Fig. 3c) showed a broad peak centered at 20.4° (silk II structure, β-sheet crystals) with a shoulder at 24.5° (silk I structure) [32,40–42]. As the concentration of AlN increased, the intensity of those two peaks gradually weakened. In addition, the full width at half maximum (FWHM) of the silk crystal peak and the silk crystal size estimated by Scherrer's formula [43,44] are provided in Table S1. The results show that the average crystal size of pure silk (in the direction perpendicular to the measuring surface) is around 4.1 nm, and as the AlN content increases to 25%, the crystal size gradually decreases to 3.6 nm.

FTIR was used to study the secondary structure of silk fibroin (Fig. 4a). Whereas the spectrum of pure AlN was featureless above 900 cm^{-1}, that of pure SF (Fig. 4a) displayed a peak at 3250 cm^{-1} caused by the *O*–H stretching vibration [31,32] in addition to multiple peaks from 900 to 1700 cm^{-1}. The amide I region of SF proteins corresponds to 1610-1700 cm^{-1} (inset Fig. 4a) [45], and pure SF spectrum had a pronounced peak at 1619 cm^{-1}, indicating a high β-sheet crystalline content after the water annealing. It needs to be noted that the spectra of the SF and AlN/SF films exhibited a predominately random coil structure prior to the water annealing procedure, with a pronounced peak at 1639 cm^{-1} (inset Fig. S4a). Through water annealing, the characteristic peaks of AlN (from 500 to 900 cm^{-1}) also shifted slightly and changed in

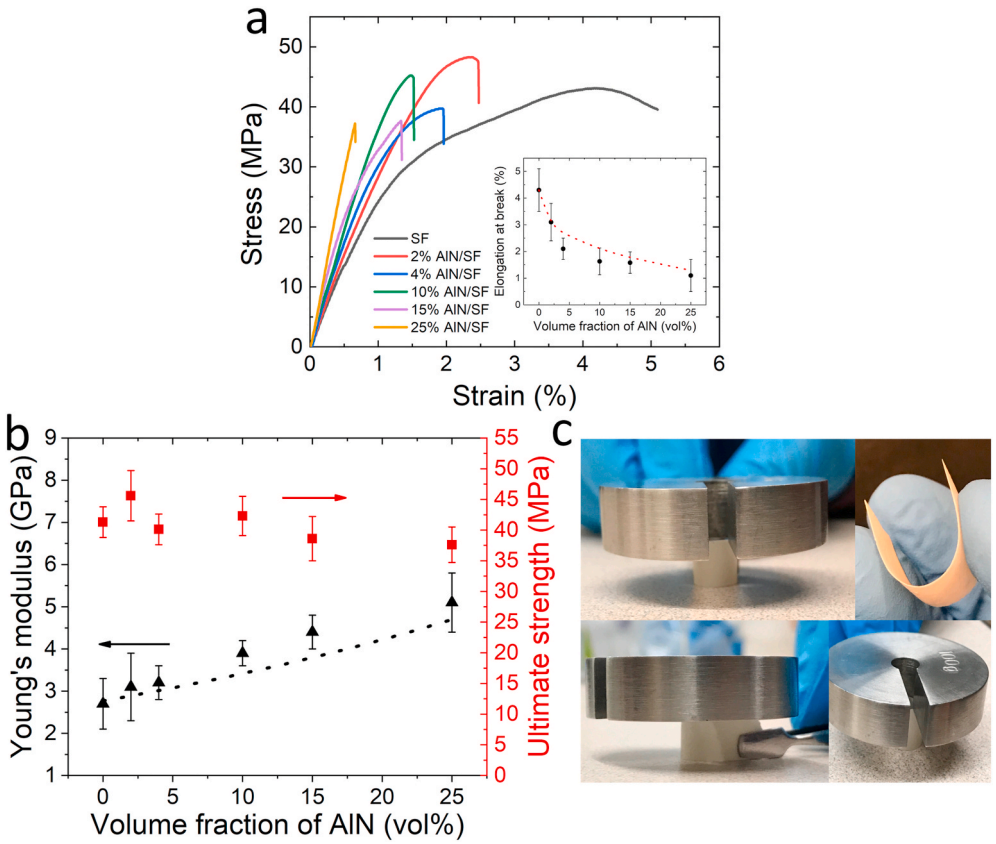

Fig. 5. (a) Representative stress-strain curves of SF and AlN/SF composites. The inset shows the elongation at break and the dotted line represents modeling results from Eqs. (S2) and (S3). (b) Dependence of the of Young's modulus and ultimate strength on the volume fraction of AlN. The dotted line represents modeling results from Eq. (3). (c) A demo picture shows a flexible single layer 10% AlN/SF is strong enough to support a 100 g weight.

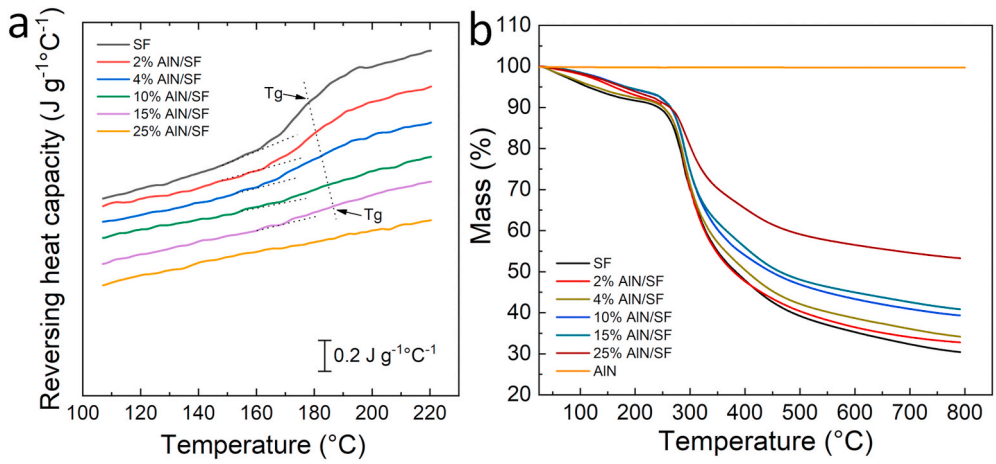

Fig. 6. (a) Temperature dependence of the reversing heat capacity of SF and AlN/SF films. (b) Temperature dependence of the mass remaining of SF, AlN/SF films and AlN.

intensity (Fig. S4a and 4a). Therefore, water annealing may not only promote the formation of strong hydrogen bonds between silk protein molecules, but also enhance the formation of hydrogen bonds between SF and AlN molecules.

Fourier self-deconvolution (FSD) method is an effective tool to calculate the secondary structure content in SF [31,40], and a curve fitting example for FSD amide I spectra of the SF sample is shown in Fig. S4b. The detailed structure contents of different SF/AlN samples are provided in Table S2 and Table S3. Results show that pure SF (after water annealing) contains 38% β-sheet crystals and 20% random coil structure. As the AlN content increased, the shoulder at 1649 cm^{-1} grew, and the peak at 1619 cm^{-1} gradually shifted to a higher value of 1625 cm^{-1} (Fig. 4a, inserted figure), indicating that the addition of AlN particles inhibited the formation of β-sheet crystals probably due to increased hydrogen bonding with the protein chains. Likewise, increased AlN promoted the random silk structure (Fig. 4b), which helps to maintain the flexibility of the composite [31,45]. Raman spectroscopy analysis performed on the amide I region of the water annealed SF/AlN sample also confirmed the results obtained from FTIR (Fig. S4c). Pure SF is dominated by β-sheet structures with a Raman peak at 1663 cm^{-1} (Fig. S4c), and with the increase of AlN content, the peak gradually shifts higher to 1669 cm^{-1}. The intensity of the Raman peaks due to β-turns and unordered random coils also increased, confirming that the AlN particles disrupted the β-sheet formation [46].

3.2. Physical properties

Fig. 5a shows the stress-strain curves of the composite, and Young's modulus steadily increased with the AlN content (Fig. 5b). Berryman [47–49] has developed a self-consistent model of the effective bulk (K_{eff}) and shear (μ_{eff}) moduli of composites based upon the geometric means of the Hashin-Shtrikman bounds [50,51]: i.e. $K_{eff} = \sqrt{K_{HS}^{+}K_{HS}^{-}}$, $\mu_{eff} = \sqrt{\mu_{HS}^{+}\mu_{HS}^{-}}$ where

$$K_{HS}^{\pm} = K_m + \frac{f}{(K_i - K_m)^{-1} + (1-f)\left(K_m + \frac{4}{3}\mu_m\right)^{-1}} \quad (1)$$

And

$$\mu_{HS}^{\pm} = \mu_m + \frac{f}{(\mu_i - \mu_m)^{-1} + \frac{2(1-f)(K_m+2\mu_m)}{5\mu_m\left(K_m+\frac{4}{3}\mu_m\right)}} \quad (2)$$

With K_{HS} (μ_{HS}) being the upper and lower bounds of the bulk (shear) modulus for the composite, K_m (μ_m) the bulk (shear) modulus of the matrix, K_i (μ_i) the bulk (shear) modulus of the inclusions, and f the volume fraction of the inclusions. Consequently, the effective Young's modulus E_{eff} is given by

$$E_{eff} = \frac{9K_{eff}\mu_{eff}}{(3K_{eff} + \mu_{eff})} \quad (3)$$

The bulk modulus of silk and AlN are 4.5 and 200 GPa [52–54], respectively, while the shear modulus of silk and AlN are 1 and 120 GPa [52–54], respectively. Previous measurements have shown that the modulus of silk is the same for crystallized and amorphous phases [55–57]. This yields the dashed line in Fig. 5b which is in good agreement with the experimental results. Note that the 10% AlN/SF sample is strong enough to support 100-g weight, which is over thousand times of its own weight (Fig. 5c).

We model the ultimate strain by assuming that it is controlled by the SF (see details in supporting information). That is the ultimate strain of each composite should be proportional to the average distance between two single AlN particles if the failure is due to SF and not due to failure of the bond between the SF and the AlN. The experimental data fit well with the model (Fig. 5a and b). In particular, given that the strains on the order of 1%, there is no slippage of the bond between the SF matrix and the AlN particles, confirming that the SF and AlN are tightly bound.

The temperature dependence of the DSC heat flow and reversing heat capacity are shown in Fig. S5a and Fig. 6a, respectively. All samples have a similar bound water evaporation peak (T_w) in Fig. S5a near 31 °C (summarized in Table 1) due to the water annealing procedure, followed by a major degradation peak around 260 °C. The glass transition steps showed in Fig. 6a are attributed to the reversible transitions of mobile amorphous component in the materials, from the frozen state to rubbery state as the temperature goes up. Previous studies have shown that silk

Table 1
Thermal analysis data from DSC and TGA.

Sample	T_g (°C)	T_w (°C)	T_{d1} (°C)	T_{d2} (°C)	Mass fraction at 800 °C (%)
SF	177.3	31.2	207.6	390.1	30.4
2% AlN/SF	180.4	31.0	223.8	387.2	32.8
4% AlN/SF	183.5	30.6	214.2	388.9	34.2
10% AlN/SF	184.3	31.8	226.3	385.6	39.3
15% AlN/SF	186.4	31.4	224.1	373.3	40.9
25% AlN/SF	N/A	31.0	230.1	366.6	53.3

*N/A indicate the value was undetermined; All numbers have an error of less than ±1 °C.

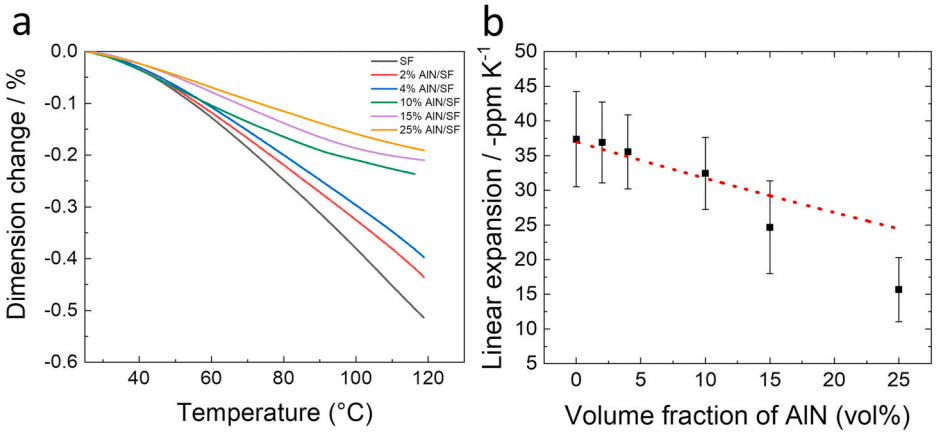

Fig. 7. (a) Dimension change of SF and AlN/SF composites with a function of temperature. (b) Linear thermal expansion of AlN/SF films as a function of AlN. The dotted line represents modeling results from Eq. (4).

fibers have a glass transition temperature T_g near 176 °C [29,58,59]. The value of T_g increased with the AlN concentration, and the glass transition steps in the heat capacity decreased (Fig. 6a & Table 1). This suggests the mobility of long-range molecular motion of the polymer network is reduced, which provides another indication of the formation of AlN/SF continuous network structure. By 25% AlN, there was no clear indication of a glass transition even though the volume fraction of random coils in the composite remained constant at about 20%.

To further investigate the thermal stability of the composites, TGA (Fig. 6b and Fig. S5b) was used to determine the mass loss during heating as a function of temperature. Fig. 6b shows that the thermal stability of samples increased with the AlN concentration. Thus, the weight remaining percentage at 800 °C increased with the increase of AlN content in SF matrix (Table 1). For all samples, a multi-step mass loss can be observed (Fig. S5b), with two major degradation peaks (T_{d1} and T_{d2}). T_{d1} increased with increasing AlN content, while T_{d2} decreased with increasing AlN content in SF matrix (Table 1). Although it is difficult to determine which component is degrading in the two peaks of the AlN/SF samples, the shift of the degradation peaks clearly suggests that the strong interaction between SF and AlN has changed the thermal stability of the composites.

The thermal expansion is shown in Fig. 7a and b. The pure SF sample showed a negative linear expansion of −37 ppm K^{-1} [60]. With increasing AlN concentration, the magnitude of the coefficient of thermal expansion decreased, with 25% AlN having a value of −15.7 ppm K^{-1}, which is much lower than that of traditional polymers [10,61]. The dashed line is a linear fit to the data which is compared with the model of Gibiansky and Torquato for the effective coefficient of thermal expansion α_{eff} given by

$$\alpha_{eff} = \frac{\alpha_m K_m (K_{eff} - K_i) + \alpha_i K_i (K_m - K_{eff})}{K_{eff}(K_m - K_i)} \quad (4)$$

With K_{eff} being the effective bulk (shear) modulus of composites, K_i and K_m the bulk (shear) modulus of the AlN inclusions and matrix, respectively; α_i and α_m the coefficients of thermal expansion of the AlN inclusions and pure SF matrix, respectively [62–64]. It is notable that the deviation from the model is not sizable but it is significant. The fact that the elastic modulus follows the theory while the magnitude of the thermal expansion is less than expected may be an indication that there is enhanced bonding between the AlN particles [65], which prevents the thermal expansion of the SF matrix. Since the model uses the value for α_m for pure SF, which has the highest crystalline content and therefore a lower magnitude for α_m than the actual SF content in the composites, the model perhaps underestimates the magnitude of α_{eff}.

The thermal conductivity κ of the pure SF film in the in-plane direction (Fig. S7) was 0.28 W $m^{-1}K^{-1}$ [23,66–69] while AlN has a high

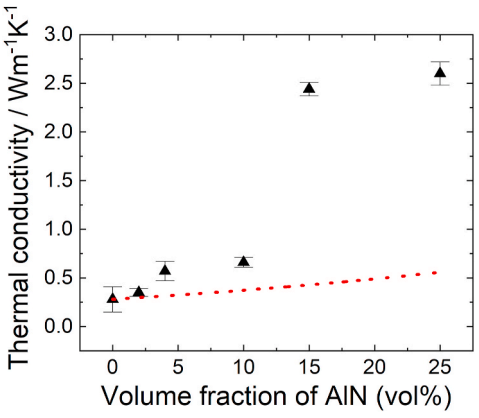

Fig. 8. Thermal conductivity of SF and AlN/SF films. The dotted line represents modeling values from the Maxwell-Garnet theory, Eq. (5).

thermal conductivity of ~320 W $m^{-1}K^{-1}$ [18–20], and thus the composites have larger κ values than SF does (Fig. 8). Assuming that one can ignore interfacial thermal resistance, one can model the thermal conductivity of an isotropic system via the Maxwell Garnett equation [70].

$$\kappa_{eff} = \kappa_m \frac{2f(\kappa_i - \kappa_m) + \kappa_i + 2\kappa_m}{2\kappa_m + \kappa_i - f(\kappa_i - \kappa_m)} \quad (5)$$

where κ_{eff} is the effective thermal conductivity of the AlN/SF film, κ_m the thermal conductivity of the matrix, and κ_i the thermal conductivity of the inclusions. The predicted values are low because the SF matrix is thermally insulating and there is no significant contribution to κ by the AlN until percolation, which occurs at $f = 1/3$ for the present model. Note that the deviation of the data from the model is particularly sizable. There are numerous reasons why the model may overestimate the value of κ, including interfacial scattering and size effects, but the unusual underestimate is most likely due to percolating networks of AlN particles in the SF as seen in Fig. 2.

To investigate this in more detail, pure SF and 25% AlN/SF samples were coated by magnetron sputtering with a layer of patterned copper of 1 μm thick (see Fig. 9). Leads were attached to the copper and both samples were subjected 0.1 W of ohmic heating. When the heat distribution on both samples reached the steady state, the temperature at the center of pure SF was nearly 70 °C, which is much higher than the 35 °C found for the 25% AlN/SF sample. This result is in accord with the tenfold increase in κ from the pure SF to 25% AlN/SF film since thermal gradient is proportional to the in-plane conductivity for this geometry [71,72].

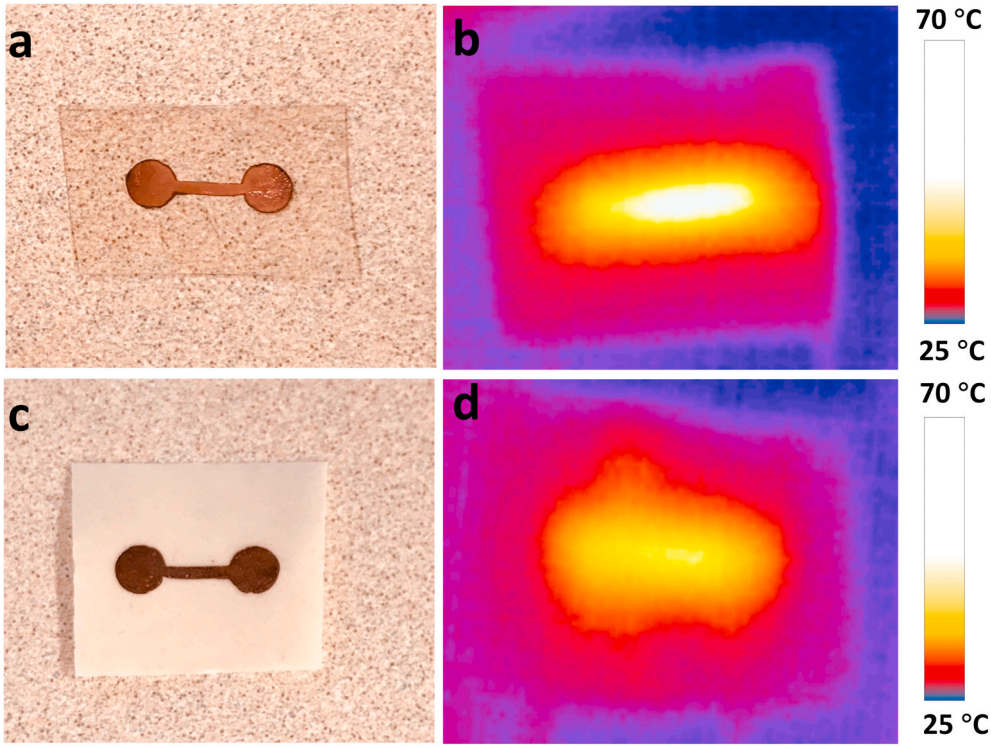

Fig. 9. Both the SF and 25% AlN/SF were coated with a copper film of about 1 μm in thickness. Leads were attached to the contact pads and 0.1 W of power was supplied for 5 min. (a) and (c) are images of SF and 25% AlN/SF samples coated with the patterned copper thin films. (b) and (d) are the thermal images of SF and 25% AlN/SF sample, respectively.

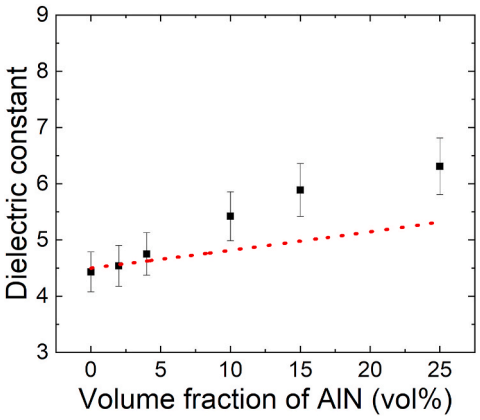

Fig. 10. Dielectric constant of SF and AlN/SF composites at 75 kHz. The dotted line represents the expected values from Maxwell-Garnet theory, Eq. (6).

The dielectric properties of SF and AlN/SF composites were also investigated to further investigate the particle structure. Fig.S6 shows the frequency dependence of the dielectric constant and loss tangent at room temperature. The real part of the dielectric constant ε as a function of AlN content is shown in Fig. 10 (also see Fig. S6), which increased with the increase of AlN content. It also was modeled with the Maxwell Garnett equation:

$$\varepsilon_{eff} = \varepsilon_m \frac{2f(\varepsilon_i - \varepsilon_m) + \varepsilon_i + 2\varepsilon_m}{2\varepsilon_m + \varepsilon_i - f(\varepsilon_i - \varepsilon_m)} \quad (6)$$

where ε_{eff} is the effective dielectric constant of the composite, ε_m the dielectric constant of the SF matrix, and ε_i the dielectric constant of the AlN inclusions.

The agreement is reasonable except for the highest AlN content, where the measured value is somewhat larger than the predicted one. That difference might be related to enhancement due to a decrease in the effective depolarization factor of the AlN particles which arises when the particles form networks. Alternatively, one must also recall that the amorphous component of SF has a larger dielectric than the crystalline form [55,63]. That may also contribute to larger value of ε of the composite, although it is unlikely to be the predominant factor.

3.3. Fire-retardance

Materials with good flame retardancy have a wider range of application. Fig. 11a shows that the pure SF sample ignited after 1s and burned throughout the duration and eventually bent. The 25% AlN/SF composite showed significantly better fire resistance. The film retained its original shape after burning for more than 20 min. The AlN particles distributed in the SF substrate make it more flame retardant and this may be enhanced by the AlN/SF network (Figure S8 in Supplemental Information). Accordingly, the TGA results also show that at 800 °C, AlN/SF has more residue as the concentration of AlN increases (Table 1).

3.4. Mechanism

There is clear interaction between the SF and the AlN, probably due to the formation of hydrogen bonds between the N atoms in AlN and SF proteins. According to the SEM and EDS data, it is believed that the AlN particles distribute homogeneously at lower concentration. However, at higher concentration, the AlN particles formed a continuous network. Fig. 12 shows a schematic of the proposed secondary structure of the composite. X-ray studies show that the SF and AlN particles are randomly oriented, but the particles are tightly bound to SF fiber by hydrogen bonding as evidenced by the trend in the glass transition temperature and the coefficient of thermal expansion. In particular, the behavior of the glass transition behavior is consistent with AlN forming a network which encapsulates the amorphous component. This network

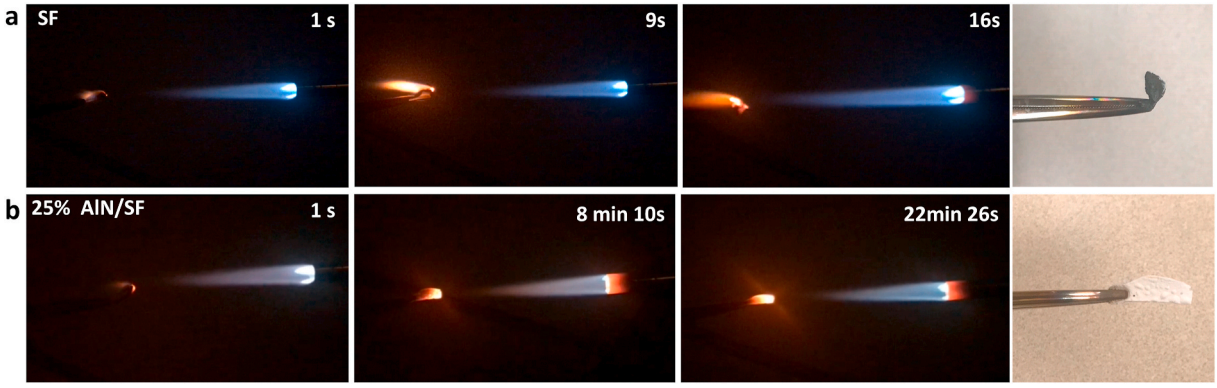

Fig. 11. Fire-retardant properties of AlN/SFfilms. Photographs of (a) SF and (b) AlN/SF 25% films heated by a flame torch at different times.

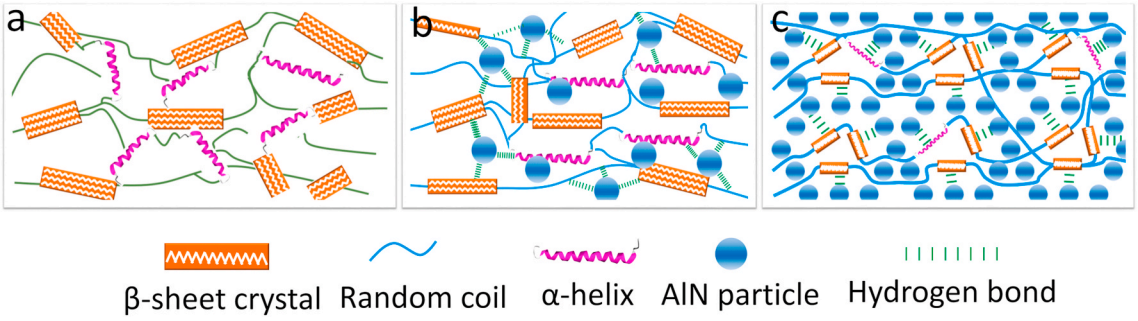

Fig. 12. Schematic diagram of secondary structure of (a) silk fibroin, and distribution of AlN in (b) 10% AlN/SF and (c) 25% AlN/SF, respectively.

structure and hydrogen bonding are central to the significantly enhanced thermal conductivity [27] of the composites.

4. Conclusion

In summary, this study investigated the physical and structural properties of AlN/SF composites. We found layered structures in the cross section of the AlN/SF films. In the SF component, the content of the β-sheet crystal decreases as the AlN content increases. AlN/SF has good thermal stability, low linear thermal expansion, and higher stiffness while maintaining flexibility. The 25% AlN/SF has a negative linear thermal expansion of at -15.7 ppm K^{-1}. The thermal conductivity of AlN/SF is also significantly enhanced, which results from AlN forming networks to provide paths of low thermal resistance and is aided by the strong hydrogen bonding between the AlN and SF to reduce the interfacial phonon scattering. This work demonstrates that there can be significant interaction between organic and inorganic phases in composite materials, and the effects can be synergistic to create greatly enhanced materials which can be tailored for a variety of applications.

Funding source

This study was supported in part by the Rowan University Start-up Grants. X.H. is also supported by the US NSF Biomaterials Program (DMR-1809541).

CRediT authorship contribution statement

Ye Xue: Formal analysis, Validation, Investigation, Writing - original draft, Visualization. **Samuel Lofland:** Conceptualization, Methodology, Supervision, Data curation, Writing - review & editing, Resources. **Xiao Hu:** Conceptualization, Methodology, Validation, Supervision, Project administration, Formal analysis, Funding acquisition, Writing - review & editing, Resources.

Declaration of competing interest

The authors declare that they have no known competing financial interests or personal relationships that could have appeared to influence the work reported in this paper.

Acknowledgements

We thank Dr. Jeffrey Hettinger for assistance in the deposition of the copper.

Appendix A. Supplementary data

Supplementary data to this article can be found online at https://doi.org/10.1016/j.compositesb.2020.108377.

References

[1] Wu Y, Xue Y, Qin S, Liu D, Wang X, Hu X, et al. BN nanosheet/polymer films with highly anisotropic thermal conductivity for thermal management applications. ACS Appl Mater Interfaces 2017;9(49):43163–70.
[2] Hu J, Huang Y, Yao Y, Pan G, Sun J, Zeng X, et al. Polymer composite with improved thermal conductivity by constructing a hierarchically ordered three-dimensional interconnected network of BN. ACS Appl Mater Interfaces 2017;9(15):13544–53.
[3] Barani Z, Mohammadzadeh A, Geremew A, Huang CY, Coleman D, Mangolini L, et al. Thermal properties of the binary-filler hybrid composites with graphene and copper nanoparticles. Adv Funct Mater 2020;30(8):1904008.
[4] Wang J, Wu Y, Xue Y, Liu D, Wang X, Hu X, et al. Super-compatible functional boron nitride nanosheets/polymer films with excellent mechanical properties and ultra-high thermal conductivity for thermal management. J Mater Chem C 2018;6(6):1363–9.
[5] Chang C, Fennimore A, Afanasiev A, Okawa D, Ikuno T, Garcia H, et al. Isotope effect on the thermal conductivity of boron nitride nanotubes. Phys Rev Lett 2006;97(8):085901.
[6] Yu J, Huang X, Wu C, Wu X, Wang G, Jiang P. Interfacial modification of boron nitride nanoplatelets for epoxy composites with improved thermal properties. Polymer 2012;53(2):471–80.

[7] Guan C, Qin Y, Li L, Wang M, Lin C-T, He X, et al. Highly thermally conductive polymer composites with barnacle-like nano-crystalline Diamond@ Silicon carbide hybrid architecture. Compos B Eng 2020:108167.
[8] Li M, Wang M, Hou X, Zhan Z, Wang H, Fu H, et al. Highly thermal conductive and electrical insulating polymer composites with boron nitride. Compos B Eng 2020; 184:107746.
[9] Guo S, Zheng R, Jiang J, Yu J, Dai K, Yan C. Enhanced thermal conductivity and retained electrical insulation of heat spreader by incorporating alumina-deposited graphene filler in nano-fibrillated cellulose. Compos B Eng 2019;178:107489.
[10] Xue Y, Zhou X, Zhan T, Jiang B, Guo Q, Fu X, et al. Densely interconnected porous BN frameworks for multifunctional and isotropically thermoconductive polymer composites. Adv Funct Mater 2018;28(29):1801205.
[11] Fujii M, Zhang X, Takahashi K. Measurements of thermal conductivity of individual carbon nanotubes. Phys Status Solidi 2006;243(13):3385–9.
[12] Mazov I, Burmistrov I, Il'inykh I, Stepashkin A, Kuznetsov D, Issi JP. Anisotropic thermal conductivity of polypropylene composites filled with carbon fibers and multiwall carbon nanotubes. Polym Compos 2015;36(11):1951–7.
[13] Fang Y, Xiong S, Huang H, Zhu J, Yu J, Wang Y, et al. Polydopamine nanotube for dual bio-inspired strong, tough, and flame retarding composites. Compos B Eng 2020:108184.
[14] Malekpour H, Balandin AA. Raman-based technique for measuring thermal conductivity of graphene and related materials. J Raman Spectrosc 2018;49(1): 106–20.
[15] Shtein M, Nadiv R, Buzaglo M, Kahil K, Regev O. Thermally conductive graphene-polymer composites: size, percolation, and synergy effects. Chem Mater 2015;27 (6):2100–6.
[16] Huxtable ST, Cahill DG, Shenogin S, Xue L, Ozisik R, Barone P, et al. Interfacial heat flow in carbon nanotube suspensions. Nat Mater 2003;2(11):731–4.
[17] Huang X, Iizuka T, Jiang P, Ohki Y, Tanaka T. Role of interface on the thermal conductivity of highly filled dielectric epoxy/AlN composites. J Phys Chem C 2012; 116(25):13629–39.
[18] Yanagida T, Fujimoto Y, Kawaguchi N, Yanagida S. Dosimeter properties of AlN. J Ceram Soc Jpn 2013;121(1420):988–91.
[19] Xu Y, Chung D, Mroz C. Thermally conducting aluminum nitride polymer-matrix composites. Compos Appl Sci Manuf 2001;32(12):1749–57.
[20] Kim Y, Ahn C-W, Choi J-J, Ryu J, Kim J-W, Yoon W-H, et al. Next generation ceramic substrate fabricated at room temperature. Sci Rep 2017;7(1):1–10.
[21] Pan C, Kou K, Zhang Y, Li Z, Wu G. Enhanced through-plane thermal conductivity of PTFE composites with hybrid fillers of hexagonal boron nitride platelets and aluminum nitride particles. Compos B Eng 2018;153:1–8.
[22] Ling S, Kaplan DL, Buehler MJ. Nanofibrils in nature and materials engineering. Nat Rev Mater 2018;3(4):1–15.
[23] Xue Y, Lofland S, Hu X. Thermal conductivity of protein-based materials: a review. Polymers 2019;11(3):456.
[24] Agari Y, Ueda A, Nagai S. Thermal conductivity of a polymer composite. J Appl Polym Sci 1993;49(9):1625–34.
[25] Wang X, Wu P. Preparation of highly thermally conductive polymer composite at low filler content via a self-assembly process between polystyrene microspheres and boron nitride nanosheets. ACS Appl Mater Interfaces 2017;9(23):19934–44.
[26] Xu X, Zhou J, Chen J. Thermal transport in conductive polymer–based materials. Adv Funct Mater 2020;30(8):1904704.
[27] Jiang F, Cui S, Song N, Shi L, Ding P. Hydrogen bond-regulated boron nitride network structures for improved thermal conductive property of polyamide-imide composites. ACS Appl Mater Interfaces 2018;10(19):16812–21.
[28] Shen H, Guo J, Wang H, Zhao N, Xu J. Bioinspired modification of h-BN for high thermal conductive composite films with aligned structure. ACS Appl Mater Interfaces 2015;7(10):5701–8.
[29] Stanton J, Xue Y, Waters JC, Lewis A, Cowan D, Hu X, et al. Structure–property relationships of blended polysaccharide and protein biomaterials in ionic liquid. Cellulose 2017;24(4):1775–89.
[30] Lammel AS, Hu X, Park S-H, Kaplan DL, Scheibel TR. Controlling silk fibroin particle features for drug delivery. Biomaterials 2010;31(16):4583–91.
[31] Hu X, Kaplan D, Cebe P. Determining beta-sheet crystallinity in fibrous proteins by thermal analysis and infrared spectroscopy. Macromolecules 2006;39(18): 6161–70.
[32] Xue Y, Wang F, Torculas M, Lofland S, Hu X. Formic acid regenerated mori, tussah, eri, Thai, and muga silk materials: mechanism of self-assembly. ACS Biomater Sci Eng 2019;5(12):6361–73.
[33] Kim H, Kim J, Choi J, Park Y, Ki C. Characterization of silk hydrogel formed with hydrolyzed silk fibroin-methacrylate via photopolymerization. Polymer 2018;153: 232–40.
[34] Liang F-C, Huang Y-H, Kuo C-C, Cho C-J, Rwei S-P, Jia Q, et al. Thermally deposited silk fibroin as the gate dielectric layer in organic thin-film transistors based on conjugated polymer. React Funct Polym 2018;131:368–77.
[35] Wang Y, Ma R, Hu K, Kim S, Fang G, Shao Z, et al. Dramatic enhancement of graphene oxide/silk nanocomposite membranes: increasing toughness, strength, and young's modulus via annealing of interfacial structures. ACS Appl Mater Interfaces 2016;8(37):24962–73.
[36] Jin HJ, Park J, Karageorgiou V, Kim UJ, Valluzzi R, Cebe P, et al. Water-stable silk films with reduced β-sheet content. Adv Funct Mater 2005;15(8):1241–7.
[37] Qi Y, Wang H, Wei K, Yang Y, Zheng R-Y, Kim IS, et al. A review of structure construction of silk fibroin biomaterials from single structures to multi-level structures. Int J Mol Sci 2017;18(3):237.
[38] Hu X, Shmelev K, Sun L, Gil E-S, Park S-H, Cebe P, et al. Regulation of silk material structure by temperature-controlled water vapor annealing. Biomacromolecules 2011;12(5):1686–96.
[39] Liu C, Hu Z, Wu Q, Wang X, Chen Y, Sang H, et al. Vapor– solid growth and characterization of aluminum nitride nanocones. J Am Chem Soc 2005;127(4): 1318–22.
[40] Cebe P, Partlow BP, Kaplan DL, Wurm A, Zhuravlev E, Schick C. Silk I and Silk II studied by fast scanning calorimetry. Acta Biomater 2017;55:323–32.
[41] Guo C, Zhang J, Wang X, Nguyen AT, Liu XY, Kaplan DL. Comparative study of strain-dependent structural changes of silkworm silks: insight into the structural origin of strain-stiffening. Small 2017;13(47):1702266.
[42] Guo C, Zhang J, Jordan JS, Wang X, Henning RW, Yarger JL. Structural comparison of various silkworm silks: an insight into the structure–property relationship. Biomacromolecules 2018;19(3):906–17.
[43] Patterson A. The Scherrer formula for X-ray particle size determination. Phys Rev 1939;56(10):978.
[44] Holzwarth U, Gibson N. The Scherrer equation versus the'Debye-Scherrer equation. Nat Nanotechnol 2011;6(9):534.
[45] Ling S, Qi Z, Knight DP, Shao Z, Chen X. Synchrotron FTIR microspectroscopy of single natural silk fibers. Biomacromolecules 2011;12(9):3344–9.
[46] Lefevre T, Paquet-Mercier F, Rioux-Dubé JF, Pézolet M. Structure of silk by Raman spectromicroscopy: from the spinning glands to the fibers. Biopolymers 2012;97 (6):322–36.
[47] Han T, Clennell MB, Cheng AC, Pervukhina M. Are self-consistent models capable of jointly modeling elastic velocity and electrical conductivity of reservoir sandstones? Geophysics 2016;81(4):D377–82.
[48] Dvorkin J, Berryman J, Nur A. Elastic moduli of cemented sphere packs. Mech Mater 1999;31(7):461–9.
[49] Dean E. Elastic moduli of porous sintered materials as modeled by a variable-aspect-ratio self-consistent oblate-spheroidal-inclusion theory. J Am Ceram Soc 1983;66(12):847–54.
[50] Watt JP, Peselnick L. Clarification of the Hashin-Shtrikman bounds on the effective elastic moduli of polycrystals with hexagonal, trigonal, and tetragonal symmetries. J Appl Phys 1980;51(3):1525–31.
[51] Wall P. A comparison of homogenization, Hashin-Shtrikman bounds and the Halpin-Tsai equations. Appl Math 1997;42(4):245–57.
[52] Koski KJ, Akhenblit P, McKiernan K, Yarger JL. Non-invasive determination of the complete elastic moduli of spider silks. Nat Mater 2013;12(3):262–7.
[53] Zhang K, Duan H, Karihaloo BL, Wang J. Hierarchical, multilayered cell walls reinforced by recycled silk cocoons enhance the structural integrity of honeybee combs. Proc Natl Acad Sci U S Am 2010;107(21):9502–6.
[54] Wang Z, Tait K, Zhao Y, Schiferl D, Zha C, Uchida H, et al. Size-induced reduction of transition pressure and enhancement of bulk modulus of AlN nanocrystals. J Phys Chem B 2004;108(31):11506–8.
[55] Yu L, Hu X, Kaplan D, Cebe P. Dielectric relaxation spectroscopy of hydrated and dehydrated silk fibroin cast from aqueous solution. Biomacromolecules 2010;11 (10):2766–75.
[56] Yazawa K, Malay AD, Ifuku N, Ishii T, Masunaga H, Hikima T, et al. Combination of amorphous silk fiber spinning and postspinning crystallization for tough regenerated silk fibers. Biomacromolecules 2018;19(6):2227–37.
[57] Yoshioka T, Tsubota T, Tashiro K, Jouraku A, Kameda T. A study of the extraordinarily strong and tough silk produced by bagworms. Nat Commun 2019; 10(1):1–11.
[58] Xue Y, Jao D, Hu W, Hu X. Silk-silk blend materials. J Therm Anal Calorim 2017; 127(1):915–21.
[59] DeFrates K, Markiewicz T, Callaway K, Xue Y, Stanton J, Salas-de la Cruz D, et al. Structure–property relationships of Thai silk–microcrystalline cellulose biocomposite materials fabricated from ionic liquid. Int J Biol Macromol 2017;104: 919–28.
[60] Aksakal B, Akdere Ü, Günay SD, Çağın T, Taşseven Ç. Influence of repeating sequence on structural and thermal stability of crystalline domain of bombyx mori silk fibroin. Mater Res Express 2020;6(12):125356.
[61] He Y. Heat capacity, thermal conductivity, and thermal expansion of barium titanate-based ceramics. Thermochim Acta 2004;419(1–2):135–41.
[62] Gibiansky L, Torquato S. Thermal expansion of isotropic multiphase composites and polycrystals. J Mech Phys Solid 1997;45(7):1223–52.
[63] Magoshi J, Magoshi Y. Physical properties and structure of silk. II. Dynamic mechanical and dielectric properties of silk fibroin. J Polym Sci Polym Phys Ed 1975;13(7):1347–51.
[64] Magoshi J, Magoshi Y, Nakamura S, Kasai N, Kakudo M. Physical properties and structure of silk. V. Thermal behavior of silk fibroin in the random-coil conformation. J Polym Sci Polym Phys Ed 1977;15(9):1675–83.
[65] Zhi C, Bando Y, Tang C, Kuwahara H, Golberg D. Large-scale fabrication of boron nitride nanosheets and their utilization in polymeric composites with improved thermal and mechanical properties. Adv Mater 2009;21(28):2889–93.
[66] Liu G, Huang X, Wang Y, Zhang Y-Q, Wang X. Thermal transport in single silkworm silks and the behavior under stretching. Soft Matter 2012;8(38):9792–9.
[67] Liu G, Xu S, Cao TT, Lin H, Tang X, Zhang YQ, et al. Thermally induced increase in energy transport capacity of silkworm silks. Biopolymers 2014;101(10):1029–37.
[68] Park J, Kim D, Lee S-M, Choi J-U, You M, So H-M, et al. Effects of β-sheet crystals and a glycine-rich matrix on the thermal conductivity of spider dragline silk. Int J Biol Macromol 2017;96:384–91.
[69] Zhang L, Bai Z, Ban H, Liu L. Effects of the amino acid sequence on thermal conduction through β-sheet crystals of natural silk protein. Phys Chem Chem Phys 2015;17(43):29007–13.

[70] Gao L, Zhou XF. Differential effective medium theory for thermal conductivity in nanofluids. Phys Lett 2006;348(3–6):355–60.
[71] Giri A, Niemelä J-P, Tynell T, Gaskins JT, Donovan BF, Karppinen M, et al. Heat-transport mechanisms in molecular building blocks of inorganic/organic hybrid superlattices. Phys Rev B 2016;93(11):115310.
[72] Malhotra A, Maldovan M. Surface scattering controlled heat conduction in semiconductor thin films. J Appl Phys 2016;120(20):204305.